Chemical Science

ROYAL SOCIETY OF CHEMISTRY

EDGE ARTICLE

Cite this: *Chem. Sci.*, 2022, **13**, 3281

All publication charges for this article have been paid for by the Royal Society of Chemistry

Received 3rd December 2021
Accepted 23rd February 2022

DOI: 10.1039/d1sc06751f

rsc.li/chemical-science

Photoluminescent coordination polymer bulk glasses and laser-induced crystallization†

Zeyu Fan,[b] Chinmoy Das,[a] Aude Demessence,[c] Ruilin Zheng,[d] Setsuhisa Tanabe,[d] Yong-Sheng Wei[a] and Satoshi Horike *[abef]

We synthesized luminescent coordination polymer glasses composed of d^{10} metal cyanides and triphenylphosphine through melt-quenching and mechanical milling protocols. Synchrotron X-ray total scattering measurements and solid-state NMR revealed their one-dimensional chain structures and high structural dynamics. Thermodynamic and photoluminescence properties were tunable by the combination of heterometallic ions (Ag^+, Au^+, and Cu^+) in the structures. The glasses are moldable and thermally stable, and over centimeter-sized glass monoliths were fabricated by the hot-press technique. They showed high transparency over 80% from the visible to near-infrared region and strong green emission at room temperature. Furthermore, the glass-to-crystal transformation was demonstrated by laser irradiation through the photothermal effect of the glasses.

Introduction

Glassy coordination polymers (CPs) and metal–organic frameworks (MOFs) have been of interest as a new class of amorphous materials.[1–4] Their structure and properties are distinct from conventional glasses and are controlled by the combination of metal ions and bridging molecular ligands. In addition, the non-crystalline, high processability, and adhesive characteristics have gained research interest in both fundamental behaviors as well as applications such as ion conductive solid electrolytes, gas separation membranes, and electrochemical catalysis.[5–10]

One of the most successful applications of glass, in general, is optics. The transparency and moldability of optically active glass materials have enabled many optical functionalities, including photoconductivity, photon up-conversion, and spectral concentration.[11–13] However, studies on the optical properties and materials fabrication of CP/MOF glasses are still in their infancy. This is because limited compounds have been found which possess essential criteria for optical materials: (i) strong luminescence, (ii) moldability in bulk size (over a centimeter), and (iii) high transparency over 80%.[14] The preparation of bulk ZIF-62 glass monoliths with a high transparency up to 90% in the visible and near-infrared region has been reported in a previous report.[15] Mid-infrared luminescence was achieved through Co^{2+} doping into ZIF-62 glass.[16,17] Au^+ and thiophenolate CP only showed red luminescence at low-temperature (−180 °C) and a transparency of 26% at 850 nm.[18] It is demanded to explore the new luminescent CP/MOF glasses to meet these criteria.

One ligand system to construct CP/MOFs with tunable compositions and dimensionalities is cyanide.[19–21] CP/MOFs composed of cyanide and dicyanamide are reported to show melting and vitrification behaviors. The flexible coordination bond between cyanides and monovalent d^{10} metal ions is suitable for glass formation.[22–25] Here we report three cyanide-based CP glasses with one-dimensional (1D) structures $\{[\mathbf{M^N}(PPh_3)_2][\mathbf{M^C}(CN)_2]\}_n$ ($\mathbf{M^N}$, $\mathbf{M^C}$ = Cu^+, Ag^+ or Au^+).[26] The glassy state was obtained from crystalline states through either the melt-quenching or ball milling process. The alternative monovalent metal centers adjust the thermodynamic and photoluminescence properties of glasses. The CP glasses formed a centimeter-scale transparent monolith by a simple vacuum hot-press technique and showed strong green emission at room temperature. Moreover, the laser triggered phase transition from glass to the crystal in the monolith was demonstrated.

[a]*AIST-Kyoto University Chemical Energy Materials Open Innovation Laboratory (ChEM-OIL), National Institute of Advanced Industrial Science and Technology (AIST), Yoshida-Honmachi, Sakyo-ku, Kyoto 606-8501, Japan. E-mail: horike@icems.kyoto-u.ac.jp*

[b]*Department of Synthetic Chemistry and Biological Chemistry, Graduate School of Engineering, Kyoto University, Katsura, Nishikyo-ku, Kyoto 615-8510, Japan*

[c]*Univ Lyon, Claude Bernard Lyon 1 University, UMR CNRS 5256, Institute of Researches on Catalysis and Environment of Lyon (IRCELYON), Villeurbanne, France*

[d]*Graduate School of Human and Environmental Studies, Kyoto University, Kyoto 606-8501, Japan*

[e]*Institute for Integrated Cell-Material Sciences, Institute for Advanced Study, Kyoto University, Yoshida-Honmachi, Sakyo-ku, Kyoto 606-8501, Japan*

[f]*Department of Materials Science and Engineering, School of Molecular Science and Engineering, Vidyasirimedhi Institute of Science and Technology, Rayong, 21210, Thailand*

† Electronic supplementary information (ESI) available: Experimental procedures and supplementary figures, table and schemes. See DOI: 10.1039/d1sc06751f

Results and discussion

Crystal structures

Fig. 1A and B show the crystal structures of $\{[Ag(PPh_3)_2][Au(CN)_2]\}_n$ (**AgAu**).[27] Ag^+ has a tetrahedral configuration with two phosphine atoms from triphenylphosphine (PPh_3) and two nitrogen atoms from cyanides. These tetrahedra are linked to Au^+ to give 1D zig-zag chains along the *c*-axis. Weak interactions including Au···H and C–H···π interactions exist between the 1D chains. Guest-containing $\{[Ag(PPh_3)_2][Cu(CN)_2]\}_n \cdot xH_2O$ and $\{[Cu(PPh_3)_2][Au(CN)_2]\}_n \cdot xH_2O$ were synthesized as microcrystalline powders following the reported procedures (see the ESI†).[26–28] Their guest-free phases, $\{[Ag(PPh_3)_2][Cu(CN)_2]\}_n$ (**CuAg**) and $\{[Cu(PPh_3)_2][Au(CN)_2]\}_n$ (**CuAu**), were obtained by removing the guest water molecules upon heating. Powder X-ray diffraction (PXRD) patterns of **AgCu** and **CuAu** are similar to that of **AgAu**, indicating that they have the same 1D chain structures (Fig. S1A, S2A and S3A†). We conducted Rietveld refinement analysis of **AgCu** and **CuAu** using synchrotron PXRD data at 25 °C. These two crystal structures have the same space group as **AgAu**, and the structures are identical with slight differences of cell parameters (Fig. S4†). Elemental analyses and FT-IR spectra also confirmed the compositions and same structures for the three compounds. The compounds are hereafter denoted as $\mathbf{M^NM^C}$, where $\mathbf{M^C}$ is the metal center that links to the C atoms, and $\mathbf{M^N}$ is the metal center that links to the N atoms (Scheme 1).

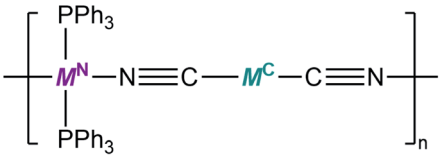

AgAu | M^N = Ag, M^C = Au
CuAu | M^N = Cu, M^C = Au
AgCu | M^N = Ag, M^C = Cu

Scheme 1 Illustration of the chemical structures of M^NM^C.

Crystal melting and formation of melt-quenched glass (MQG)

Thermogravimetric analysis (TGA) was carried out to check the thermal behaviors of $\mathbf{M^NM^C}$. **AgCu** and **CuAu** showed no weight loss at 200 °C, while **AgAu** exhibited higher thermal stability and no weight loss at 220 °C. All $\mathbf{M^NM^C}$s melt upon heating. Differential scanning calorimetry (DSC) clarified that the melting temperatures (T_m) of **AgAu**, **AgCu**, and **CuAu** are 218, 198, and 197 °C, respectively. The melt phases of **CuAu** and **AgAu** are colorless, and that of **AgCu** is yellow (Fig. S1B, S2B and S3B†). The enthalpy and entropy changes in phase transition (ΔH_m and ΔS_m) calculated from DSC are summarized in Table S1.† **AgAu** exhibits higher T_m and ΔH_m (65 kJ mol^{-1}) than **CuAu** and **AgCu**, suggesting the stronger coordination bonds and M^C···H and C–H···π interactions. Glass transition (T_g) of **CuAu** was observed at 100 °C in the first cooling process, and the second heating–cooling cycle (Fig. 1C). We denote the glassy state of **CuAu** obtained by melt-quenching as **CuAu-MQG** hereafter. Glassy materials usually exhibit a T_g/T_m (K/K) value of 2/3, which is summarized as the empirical Kauzmann 2/3 rule.[29,30] **CuAu-MQG** has a T_g/T_m value of 0.79, which is higher than the commonly observed 2/3 ratio (=0.67), indicative of its high glass forming ability.[31] **AgAu** and **AgCu** did not form glass but crystallized upon cooling as confirmed by DSC and PXRD (Fig. S5†). Although these compounds have identical crystal

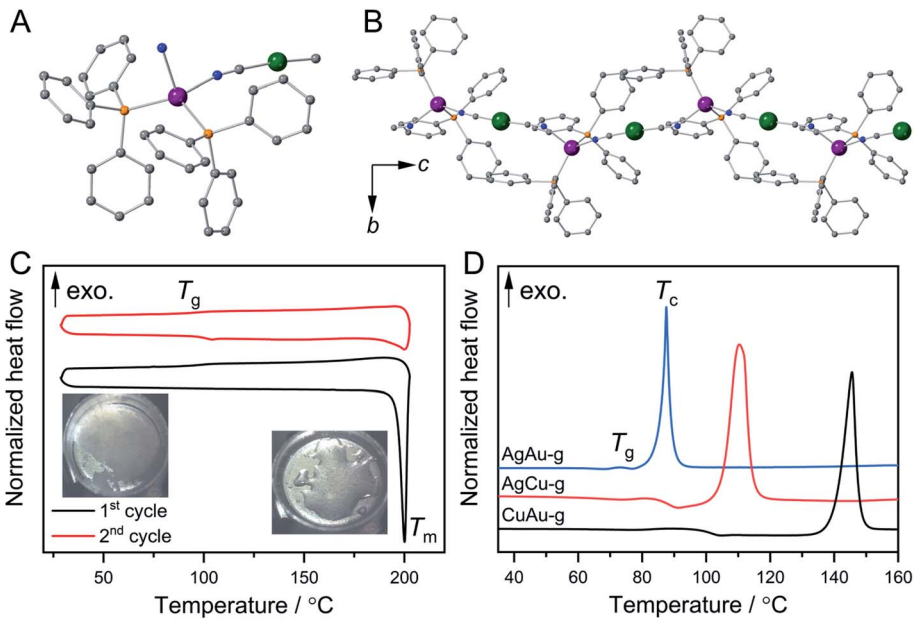

Fig. 1 Crystal structures of **AgAu** (A) in the Ag^+ coordination sphere and (B) 1D chains along the *c*-axis. Grey, blue, orange, violet, and green are C, N, P, Ag, and Au, respectively. (C) First (black) and second (red) DSC upscan/downscan cycles of **CuAu**. Melting temperature T_m and glass transition temperature T_g are shown. (D) First DSC upscan of $\mathbf{M^NM^C}$**-g** from 35 to 160 °C. The heating rate is 10 °C min^{-1}.

structures, they show different T_m and ΔH_m. Higher ΔH_m in **AgAu** and **AgCu** than in **CuAu** suggests the stronger interactions (coordination bonds and other non-covalent interactions) in coordination polymers, which result in faster recrystallization kinetics than glass formation.[32] Elemental analysis suggested that the composition of $\mathbf{M^NM^C}$s does not change by the melt-quench process (Table S2†).

Formation of mechanically induced glasses (MIGs) and thermal properties

Ball milling of CP crystals is another procedure to obtain a glassy state.[5,33] Ball milling of three $\mathbf{M^NM^C}$s under an Ar atmosphere yielded the MIGs that are denoted as $\mathbf{M^NM^C}$**-g** hereafter. $\mathbf{M^NM^C}$**-g** exhibited broad PXRD patterns suggesting their amorphous nature. TGA confirmed that the decomposition temperatures of $\mathbf{M^NM^C}$**-g** are the same as $\mathbf{M^NM^C}$ (Fig. S1–S3†). DSC confirmed that the onset T_g of $\mathbf{M^NM^C}$**-g** are 73 °C, 84 °C, and 100 °C for **AgAu-g**, **AgCu-g**, and **CuAu-g**, respectively. Above T_g, we found the exothermal peaks which correspond to crystallization. The crystallization peak temperatures (T_c) are 88 °C, 116 °C, and 146 °C for **AgAu-g**, **AgCu-g**, and **CuAu-g** (Fig. 1D). PXRD confirmed that all $\mathbf{M^NM^C}$**-g** crystallized back to the original crystal structures $\mathbf{M^NM^C}$ (Fig. S1A, S2A and S3A†). Different thermal behaviors were found between **CuAu-MQG** and **CuAu-g** in the heating process of the DSC profile, in which **CuAu-MQG** did not show T_c at 146 °C. This is due to their different particle sizes and surface areas. The larger surface area of **CuAu-g** induces higher probability for crystallization.[23] We ground **CuAu-MQG** into a powder and then performed DSC. T_g and T_c at 100 and 146 °C were observed in the first heating process of the DSC profile, which is identical to **CuAu-g**. No exothermal peak was observed in the second heating process because of the formation of the bulk melt-quenched glass (Fig. S6†). **CuAu-g** exhibited the largest temperature window between T_g and T_c of 46 °C among $\mathbf{M^NM^C}$**-g** (15 °C for **AgAu-g** and 32 °C for **AgCu-g**). The large operating window of **CuAu-g** provides an opportunity for glass engineering since crystallization hardly happens during the thermal treatment.[34]

Structural characterization of MIGs

FT-IR and Raman spectra were measured to study the local structural differences between $\mathbf{M^NM^C}$ and $\mathbf{M^NM^C}$**-g**, as the –C≡N bond (νCN) vibration is sensitive to its chemical environment.[35] The four cyanide vibration peaks in **CuAu** are due to the coupling of stretching modes between cyanide bonds.[23,36] In **CuAu-g**, these vibrational peaks were broader and red-shifted to 2158 and 2118 cm^{-1}, indicating the elongation of the M^N–N coordination bond (Fig. S7†).[37,38] Only the broadness of the νCN bands is observed in **AgCu-g** and **AgAu-g** with a negligible shift (Fig. S8 and S9†). In the Raman spectra of **CuAu**, the peak at 128.9 cm^{-1} that is assigned to Cu–P vibration disappeared by vitrification.[39,40] Same as **CuAu-g**, the peaks corresponding to Ag–P at 125.1 and 126.7 cm^{-1} in **AgCu-g** and **AgAu-g** disappeared (Fig. S10–S12†). The loss of crystallinity results in a broadening or disappearance of peaks in the Raman spectra.[41–43]

We performed X-ray absorption spectroscopy (XAS) for **CuAu** and **CuAu-g** to understand the local structure around Cu^+. They showed identical X-ray absorption near-edge structure (XANES) spectra with the intense rising-edge 1s to 4p transition lies at 8980 eV, which is identical to Cu_2O. This suggests that Cu in **CuAu-g** maintains the +1 oxidation state (Fig. S13†).[44] The radial distribution functions (RDFs), obtained from the Fourier-transformed Cu K-edge extended X-ray absorption fine structure (EXAFS) spectra, showed a similar shape in the range of 1.2 to 2.3 Å corresponding to the first coordination sphere of Cu^+. The lower peak intensity in **CuAu-g** than in **CuAu** is due to the structural disorder. The fitting results of k^3 weighted RDFs indicate that the coordination number of Cu^+ is 4.3 ± 0.6 and 4.2 ± 1.0 in **CuAu** and **CuAu-g** (Fig. S14†). The results suggest that the tetrahedral coordination geometry of Cu is preserved in the glassy state. X-ray total scattering measurements and corresponding pair distribution function (PDF) analyses were carried out to investigate the structural periodicity in $\mathbf{M^NM^C}$**-g**. We compared the PDF profile of $\mathbf{M^NM^C}$**-g** with the simulated profile of $\mathbf{M^NM^C}$. The peaks at 5.0, 9.8 (peak 1), and 13.6 Å (peak 2) in Fig. 2A of **CuAu-g** correspond to **Cu**–NC–**Au**, **Cu**–Au$(CN)_2$–**Cu**/**Au**–Cu$(NC)_2$–**Au**, and **Cu**–Au$(CN)_2$–Cu–NC–**Au** (Fig. 2A and B). This indicates the preservation of the periodic order along the 1D chain in the glassy state. PDF profiles of **AgCu-g** and **AgAu-g** showed the same periodic features as **CuAu-g** (Fig. S15†). We conclude that the 1D chain structures are mainly preserved in $\mathbf{M^NM^C}$**-g** with disordered packing modes.

Solid-state NMR (SSNMR) at 25 °C was carried out to study the structural dynamics (Fig. S16†). ^{31}P NMR spectra of **CuAu** exhibited peaks at 8.1, 3.2, −1.6, −6.6, and −12.4 ppm ascribed to Cu–P and P–P couplings. Broad peaks at −2.5 and 40 ppm were observed in **CuAu-g** due to the structural disorder. The peak at 40 ppm is ascribed to Cu$(PPh_3)_2$NC units.[45] The ^{1}H spin-lattice relaxation time (T_1) of PPh_3 in **CuAu-g** is 2.60 s, significantly shorter than that of **CuAu** (47.37 s). As a same trend, T_1 values of ^{1}H for **AgCu-g** and **AgCu** are 3.03 and 121.21 s, respectively. The shorter T_1 in $\mathbf{M^NM^C}$**-g** suggests the higher mobility of PPh_3 ligands by the smaller M^C···H and C–H···π interactions as a result of weakened inter-chain interaction.[46]

Photoluminescence properties of MIGs

The excitation and emission spectra of **CuAu** and **CuAu-g** are shown in Fig. 2C. **CuAu** showed the emission peak at 484 nm and excitation maximum at 338 nm. Previous studies have confirmed that the emission of $\mathbf{M^NM^C}$ is from metal-to-metal-to-ligand charge transfer (MMLCT).[28] The LUMO of $\mathbf{M^NM^C}$ is composed of π*(C≡N) and p*(M^N) orbitals and HOMO is composed of the d_{xy^2} orbital of the $M^NN_2P_2$ chromophore with σ(M^N–P) bonding, π-orbital from phenyl rings and π(C≡N) bonding. The excitation and emission maxima red-shifted to 367 and 500 nm in **CuAu-g**. The emission and excitation spectra of **CuAu-MQG** show the same feature as **CuAu-g** (Fig. S17A†). The alteration of coordination bond lengths and molecular packing upon glass formation would affect the electronic structures and induce different photophysical properties. The changes contribute to the different energy levels of bonding

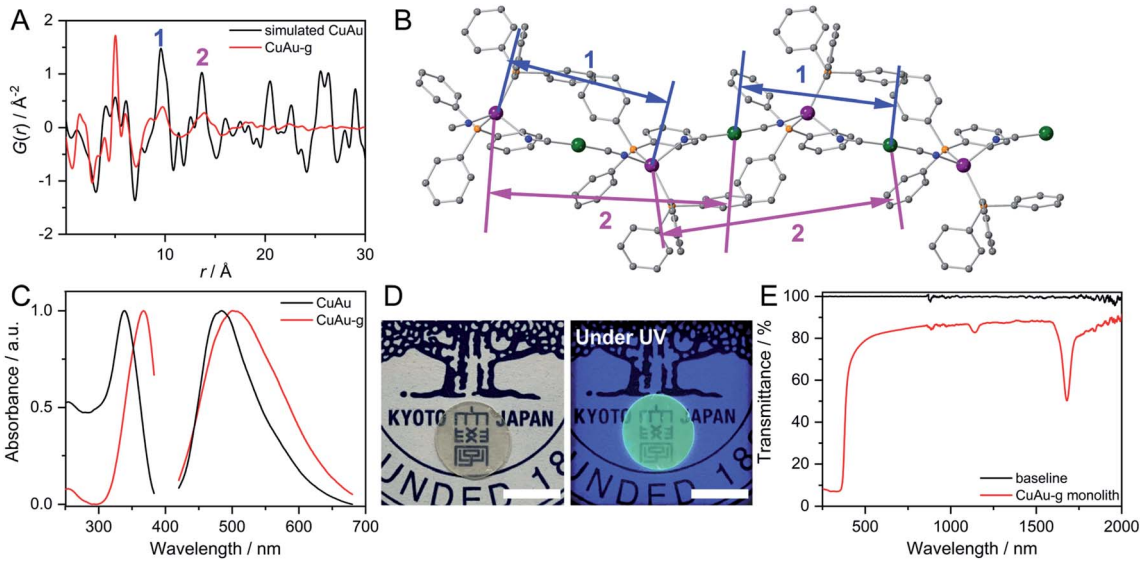

Fig. 2 (A) PDF profiles of simulated **CuAu** and **CuAu-g** at 25 °C. (B) Atomic pairs corresponding to peak 1 and 2 in the PDF profile of **CuAu**. Grey, blue, orange, violet, and green are C, N, P, Cu, and Au, respectively. (C) Excitation and emission spectra of **CuAu** and **CuAu-g** at 25 °C. (D) Transparent monolith of **CuAu-g** made by hot-pressing with/without UV light. Scale bar is 1 cm. (E) Transmittance of the **CuAu-g** monolith from 250 nm to 2000 nm.

orbitals and antibonding orbitals. This causes the smaller HOMO–LUMO bandgap and the bathochromic shift of the MMLCT emission band in **CuAu-g**.[47,48] The full width at half maximum of the emission spectra of **CuAu** and **CuAu-g** is 96 and 140 nm. The larger FWHM is consistent with its disordered structure. **AgCu**, **AgAu**, and their glassy states exhibit weaker emissions than **CuAu** and **CuAu-g**. In **AgCu** and **AgAu**, the emission band did not significantly shift by amorphization because the HOMO–LUMO band gap is kept at a similar level (Fig. S17B and C†). $\mathbf{M^NM^C}$ exhibited two-component decay of the photoluminescence lifetime in the microsecond time scale, implying the phosphorescence mechanism. **CuAu** has 22.7 μs (61.7%) and 4.6 μs (38.3%) of photoluminescence lifetimes. **CuAu-g** exhibits 8.0 μs (36.2%) and 1.4 μs (63.8%). The average photoluminescence lifetime is 15.8 μs for **CuAu** and 3.8 μs for **CuAu-g**. The shorter lifetime in a glassy state than that of the crystal is due to the following reasons. (i) Increased energy trapping states by the formation of defects and (ii) enhanced molecular dynamics in glassy states as confirmed by the relaxation time of SSNMR.[49,50] The other two glasses $\mathbf{M^NM^C}$**-g** also showed a shorter photoluminescence lifetime than $\mathbf{M^NM^C}$ (Fig. S18†).

Preparation of a transparent bulk glass monolith from MIGs and laser-induced crystallization

One of most important advantages of glass is the processability of materials in a wide range of scales. We prepared a bulk glass monolith by the vacuum hot-press technique. We first preheated the pellet of **CuAu-g** at 105 °C which is higher than its T_g (100 °C). The pressure of 60 kN was then applied to the pellet and maintained for 30 min. A bulk glass monolith with a diameter of 1.273 cm and thickness of 0.438 mm was obtained after cooling to 25 °C. The prepared **CuAu-g** monolith maintains its amorphous state as confirmed by PXRD (Fig. S19A†). It exhibits high transparency and maintains green emission under UV light irradiation (365 nm, Fig. 2D). The transmittance is over 80% from 400 to 2000 nm, comparable to soda-lime glass which is used for windows.[51–53] The absorption below 400 nm is ascribed to the MMLCT absorption band. Two absorption peaks observed at 1139 and 1680 nm are from the C–H stretching from the phenyl groups of PPh_3, as these two peaks are observed at similar wavelengths from the reflectance diffusion spectra of PPh_3 (Fig. 2E and S19B†).[54] SEM and microscope images indicate that the monolith has a crack-free and smooth surface (Fig. S20A–C†). We prepared the crystalline **CuAu** pellet under the same hot-press conditions as the control experiment. The obtained crystalline pellet was opaque, and particles separated by grain-boundaries are observed during the SEM of its surface and cross section (Fig. S20D and E†).

A similar procedure was used to prepare the transparent monolith of **AgCu-g**, and the transmittance is 80% from 400 to 2000 nm (Fig. S21†). On the other hand, the transparent monolith of **AgAu-g** was not successfully prepared because crystallization occurred during hot-pressing due to its small T_g–T_c window of 15 °C.

The phase transition from amorphous to crystal by laser irradiation is a crucial phenomenon for the preparation of glass ceramics and phase memory devices.[55–58] For instance, crystal and amorphous states of ternary alloy GeSbTe systems have different reflectance, and they are used in the Blu-ray disc. The phase transition from $\mathbf{M^NM^C}$**-g** to $\mathbf{M^NM^C}$ has been confirmed by DSC and PXRD, which inspired us to demonstrate the glass-to-crystal transformation triggered by laser irradiation. **AgCu-g** was chosen because its lower T_c (116 °C) than **CuAu-g** (T_c = 146 °C), which means less thermal energy is required to induce crystallization. We first tried to induce crystallization of **AgCu-g** by

direct irradiation of the monolith with a 730 nm laser . It was not successful due to the low absorption of the 730 nm laser in the glass. We then mixed anhydrous $CuSO_4$ (particle sizes are *ca.* 2 μm) into the glasses as the laser absorber. It is known that Cu^{2+} in $CuSO_4$ shows a photothermal effect from forbidden d–d transitions.[59,60] Homogeneous distribution of the mixed $CuSO_4$ particles would generate heat to induce the crystallization of local domains in the glasses. 20 mg of $CuSO_4$ was mixed with 180 mg of **AgCu-g** by ball-milling under an Ar atmosphere. The PXRD pattern of the mixed powder **AgCu-g-CuSO$_4$** contains characteristic peaks of only $CuSO_4$ (Fig. S22A†). Reflectance diffusion spectra of **AgCu-g-CuSO$_4$** showed an absorption band at 700 nm corresponding to the absorption of $CuSO_4$ (Fig. S22B†). The bulk monolith of **AgCu-g-CuSO$_4$** obtained by the hot-press process maintains its transparency (>60%, Fig. S21C†). $CuSO_4$ particles with a diameter of 2 μm are homogeneously distributed on the surface of the monolith, confirmed by SEM and energy-dispersive X-ray spectroscopy (EDS) mapping (Fig. S22D and E†). Fig. 3A shows the example of the surface of the monolith of **AgCu-g-CuSO$_4$** observed using the microscope. We irradiated some spots on the monolith for 60 min using a 730 nm laser of 47 μm size. The irradiated domain turned grey. Confocal Raman spectroscopy within the range of 300 nm was carried out to identify the phase of irradiated areas (Fig. 3B). The Raman spectra of grey areas 1 and 2 in Fig. 3A showed an identical pattern to **AgCu**. The Ag–P vibration peak at 125.1 cm^{-1} was found in the Raman spectra.

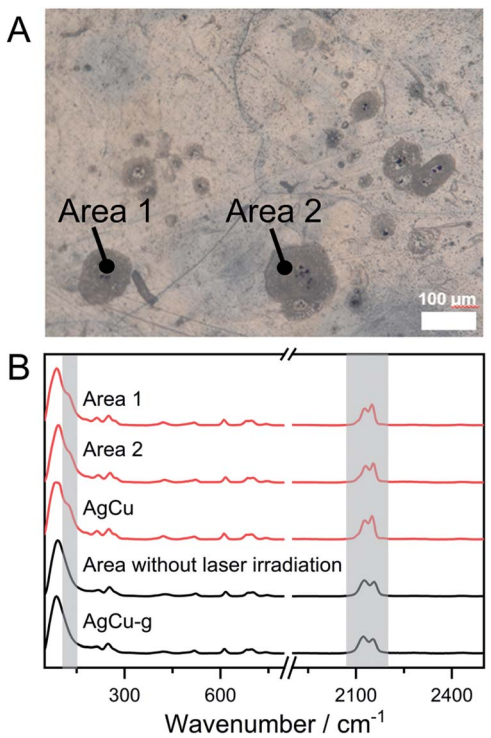

Fig. 3 (A) Surface of the **AgCu-g-CuSO$_4$** monolith under the microscope. Areas 1 and 2 are irradiated using a 47 μm size laser. Other grey spots are also crystallized domains. (B) Confocal Raman spectra at areas 1 and 2, and the area without laser irradiation. Spectra of pure **AgCu** and **AgCu-g** are also shown.

The relative intensities of the two cyanide peaks at 2130.8 and 2153.6 cm^{-1} are the same as **AgCu**. These results suggest that the crystalline **AgCu** phase was generated in areas 1 and 2 upon laser irradiation. The change was not observed in areas without laser irradiation, as also shown in Fig. 3B. This observation further proves the occurrence of glass-to-crystal transition through laser irradiation. Laser-induced crystallization was also observed on the surface of **AgCu-g-CuSO$_4$** powder pellets (Fig. S23†).

Conclusions

We have explored three luminescent CP glasses **M^{N}M^C-g** composed of d^{10} metal cyanides and triphenylphosphine. Structural analyses revealed that the glasses are constructed from 1D chains which originate from their crystal structures. Higher structural dynamics in **M^{N}M^C-g** were confirmed by solid-state NMR. The disordered structures and enhanced molecular dynamics contributed to a shorter photoluminescence lifetime of **M^{N}M^C-g** than crystalline **M^{N}M^C**. Centimeter scale glass monoliths were prepared by the hot-press technique, and they exhibited both strong emission and high transparency over 80% from 400 to 2000 nm. Furthermore, the bulk transparent glass doped with a light absorber demonstrated the laser-induced crystallization at the target spot. The strong photoluminescence at room temperature and soft, moldable character of CP/MOF glasses in micro to macro scales will provide opportunities in lighting and photonic applications.

Data availability

All data needed to evaluate the conclusions in the paper are present in the paper and supporting information. The data that support the findings of this study are available from the corresponding author upon request.

Author contributions

S. H. designed the project. Z. F. and C. D. synthesized the compounds. Z. F. conducted and analyzed PXRD, TGA, DSC, SEM, FT-IR, Raman, diffusion reflectance, photoluminescence, EXAFS, XAS and laser irradiation experiments. A. D., R. Z. and S. T. conducted and analyzed photoluminescence lifetime. Y-S. W. conducted Rietveld analysis. S. H. and Z. F. wrote the paper.

Conflicts of interest

There are no conflicts to declare.

Acknowledgements

The work was supported by the Japan Society of Promotion of Science (JSPS) for a Grant-in-Aid for Scientific Research (B) (JP21H01950) and a Grant-in-Aid for Challenging Research (Exploratory, JP19K22200) from the Ministry of Education, Culture, Sports, Science and Technology, Japan. We acknowledge Drs Kazuo Kato and Hiroki Yamada for experimental

support at Synchrotron SPring-8 BL01B1 and BL04B2 beamlines, and Dr Takahiro Fujiwara for his support in laser irradiation experiments.

References

1 S. Horike, S. S. Nagarkar, T. Ogawa and S. Kitagawa, *Angew. Chem., Int. Ed.*, 2020, **59**, 6652–6664.
2 T. D. Bennett, F. X. Coudert, S. L. James and A. I. Cooper, *Nat. Mater.*, 2021, **20**, 1179–1187.
3 J. Fonseca, T. Gong, L. Jiao and H.-L. Jiang, *J. Mater. Chem. A*, 2021, **9**, 10562–10611.
4 S. Horike, N. Ma, Z. Fan, S. Kosasang and M. M. Smedskjaer, *Nano Lett.*, 2021, **21**, 6382–6390.
5 W. Chen, S. Horike, D. Umeyama, N. Ogiwara, T. Itakura, C. Tassel, Y. Goto, H. Kageyama and S. Kitagawa, *Angew. Chem., Int. Ed.*, 2016, **55**, 5195–5200.
6 T. Ogawa, K. Takahashi, S. S. Nagarkar, K. Ohara, Y. L. Hong, Y. Nishiyama and S. Horike, *Chem. Sci.*, 2020, **11**, 5175–5181.
7 N. Ma, S. Kosasang, A. Yoshida and S. Horike, *Chem. Sci.*, 2021, **12**, 5818–5824.
8 Y. Wang, H. Jin, Q. Ma, K. Mo, H. Mao, A. Feldhoff, X. Cao, Y. Li, F. Pan and Z. Jiang, *Angew. Chem., Int. Ed.*, 2020, **59**, 4365–4369.
9 J. Li, J. Wang, Q. Li, M. Zhang, J. Li, C. Sun, S. Yuan, X. Feng and B. Wang, *Angew. Chem., Int. Ed.*, 2021, **60**, 21304–21309.
10 R. Lin, X. Li, A. Krajnc, Z. Li, M. Li, W. Wang, L. Zhuang, S. Smart, Z. Zhu, D. Appadoo, J. R. Harmer, Z. Wang, A. G. Buzanich, S. Beyer, L. Wang, G. Mali, T. D. Bennett, V. Chen and J. Hou, *Angew. Chem., Int. Ed.*, 2022, **61**, e202112880.
11 G. Yu, C. H. Lee, D. Mihailovic, A. J. Heeger, C. Fincher, N. Herron and E. M. McCarron, *Phys. Rev. B Condens Matter.*, 1993, **48**, 7545–7553.
12 J. Zhao, X. Zheng, E. P. Schartner, P. Ionescu, R. Zhang, T. L. Nguyen, D. Jin and H. Ebendorff-Heidepriem, *Adv. Opt. Mater.*, 2016, **4**, 1507–1517.
13 F. Meinardi, F. Bruni and S. Brovelli, *Nat. Rev. Mater.*, 2017, **2**, 17072.
14 F. Meinardi, S. Ehrenberg, L. Dhamo, F. Carulli, M. Mauri, F. Bruni, R. Simonutti, U. Kortshagen and S. Brovelli, *Nat. Photonics*, 2017, **11**, 177–185.
15 A. Qiao, H. Tao, M. P. Carson, S. W. Aldrich, L. M. Thirion, T. D. Bennett, J. C. Mauro and Y. Yue, *Opt. Lett.*, 2019, **44**, 1623–1625.
16 L. Frentzel-Beyme, M. Kloß, R. Pallach, S. Salamon, H. Moldenhauer, J. Landers, H. Wende, J. Debus and S. Henke, *J. Mater. Chem. A*, 2019, **7**, 985–990.
17 M. A. Ali, J. Ren, T. Zhao, X. Liu, Y. Hua, Y. Yue and J. Qiu, *ACS Omega*, 2019, **4**, 12081–12087.
18 S. Vaidya, O. Veselska, A. Zhadan, M. Diaz-Lopez, Y. Joly, P. Bordet, N. Guillou, C. Dujardin, G. Ledoux, F. Toche, R. Chiriac, A. Fateeva, S. Horike and A. Demessence, *Chem. Sci.*, 2020, **11**, 6815–6823.
19 J. F. Keggin and F. D. Miles, *Nature*, 1936, **137**, 577–578.
20 J. A. Hill, A. L. Thompson and A. L. Goodwin, *J. Am. Chem. Soc.*, 2016, **138**, 5886–5896.
21 M. J. Cliffe, E. N. Keyzer, M. T. Dunstan, S. Ahmad, M. F. L. De Volder, F. Deschler, A. J. Morris and C. P. Grey, *Chem. Sci.*, 2019, **10**, 793–801.
22 D. Venkataraman, S. Lee, J. S. Moore, P. Zhang, K. A. Hirsch, G. B. Gardner, A. C. Covey and C. L. Prentice, *Chem. Mater.*, 1996, **8**, 2030–2040.
23 C. Das, T. Ogawa and S. Horike, *Chem. Commun.*, 2020, **56**, 8980–8983.
24 C. Das and S. Horike, *Faraday Discuss.*, 2021, **225**, 403–413.
25 B. K. Shaw, A. R. Hughes, M. Ducamp, S. Moss, A. Debnath, A. F. Sapnik, M. F. Thorne, L. N. McHugh, A. Pugliese, D. S. Keeble, P. Chater, J. M. Bermudez-Garcia, X. Moya, S. K. Saha, D. A. Keen, F. X. Coudert, F. Blanc and T. D. Bennett, *Nat. Chem.*, 2021, **13**, 778–785.
26 M. Ghazzali, M. H. Jaafar, S. Akerboom, A. Alsalme, K. Al-Farhan and J. Reedijk, *Inorg. Chem. Commun.*, 2013, **36**, 18–21.
27 M. Ghazzali, M. H. Jaafar, K. Al-Farhan, S. Akerboom and J. Reedijk, *Inorg. Chem. Commun.*, 2012, **20**, 188–190.
28 M. Jaafar, A. Pevec, S. Akerboom, A. Alsalme, K. Al-Farhan, M. Ghazzali and J. Reedijk, *Inorg. Chim. Acta*, 2014, **423**, 233–237.
29 K. Ito, C. T. Moynihan and C. A. Angell, *Nature*, 1999, **398**, 492–495.
30 G. N. Greaves and S. Sen, *Adv. Phys.*, 2007, **56**, 1–166.
31 A. Qiao, T. D. Bennett, H. Tao, A. Krajnc, G. Mali, C. M. Doherty, A. W. Thornton, J. C. Mauro, G. N. Greaves and Y. Yue, *Sci. Adv.*, 2018, **4**, eaao6827.
32 M. Liu, R. D. McGillicuddy, H. Vuong, S. Tao, A. H. Slavney, M. I. Gonzalez, S. J. L. Billinge and J. A. Mason, *J. Am. Chem. Soc.*, 2021, **143**, 2801–2811.
33 Y. Ohara, A. Hinokimoto, W. Chen, T. Kitao, Y. Nishiyama, Y. L. Hong, S. Kitagawa and S. Horike, *Chem. Commun.*, 2018, **54**, 6859–6862.
34 M. L. F. Nascimento, L. A. Souza, E. B. Ferreira and E. D. Zanotto, *J. Non-Cryst. Solids*, 2005, **351**, 3296–3308.
35 K. I. Hadjiivanov, D. A. Panayotov, M. Y. Mihaylov, E. Z. Ivanova, K. K. Chakarova, S. M. Andonova and N. L. Drenchev, *Chem. Rev.*, 2021, **121**, 1286–1424.
36 A. A. Schilt, *Inorg. Chem.*, 2002, **3**, 1323–1325.
37 M. Shao, M.-X. Li, Z.-X. Wang, X. He and H.-H. Zhang, *Cryst. Growth Des.*, 2017, **17**, 6281–6290.
38 H. Yoshino, K. Yamagami, H. Wadati, H. Yamagishi, H. Setoyama, S. Shimoda, A. Mishima, B. Le Ouay, R. Ohtani and M. Ohba, *Inorg. Chem.*, 2021, **60**, 3338–3344.
39 G. B. Deacon and J. H. S. Green, *Spectrochim. Acta, Part A*, 1968, **24**, 845–852.
40 D. A. Edwards and R. Richards, *Spectrochim. Acta, Part A*, 1978, **34**, 167–171.
41 G. Wang, Y. Ling, H. Wang, X. Yang, C. Wang, J. Z. Zhang and Y. Li, *Energy Environ. Sci.*, 2012, **5**, 6180–6187.
42 H. Cui, W. Zhao, C. Yang, H. Yin, T. Lin, Y. Shan, Y. Xie, H. Gu and F. Huang, *J. Mater. Chem. A*, 2014, **2**, 8612–8616.
43 Y. Li, P. Yan, C. Guo and Q. Xu, *Chem. Commun.*, 2020, **56**, 7805–7808.

44 N. C. Tomson, K. D. Williams, X. Dai, S. Sproules, S. DeBeer, T. H. Warren and K. Wieghardt, *Chem. Sci.*, 2015, **6**, 2474–2487.
45 G. A. Bowmaker, J. C. Dyason, P. C. Healy, L. M. Engelhardt, C. Pakawatchai and A. H. White, *J. Chem. Soc., Dalton Trans.*, 1987, 1089–1097.
46 S. S. Nagarkar, H. Kurasho, N. T. Duong, Y. Nishiyama, S. Kitagawa and S. Horike, *Chem. Commun.*, 2019, **55**, 5455–5458.
47 H. Araki, K. Tsuge, Y. Sasaki, S. Ishizaka and N. Kitamura, *Inorg. Chem.*, 2005, **44**, 9667–9675.
48 E. Kwon, J. Kim, K. Y. Lee and T. H. Kim, *Inorg. Chem.*, 2017, **56**, 943–949.
49 C. L. Whittington, L. Wojtas and R. W. Larsen, *Inorg. Chem.*, 2014, **53**, 160–166.
50 M. A. Syzgantseva, N. F. Stepanov and O. A. Syzgantseva, *J. Phys. Chem. Lett.*, 2019, **10**, 5041–5046.
51 J. M. Florence, F. W. Glaze, C. H. Hahner and R. Stair, *J. Am. Ceram. Soc.*, 1948, **31**, 328–331.
52 M. Rubin, *Sol. Energy Mater.*, 1985, **12**, 275–288.
53 P. Němec, M. Olivier, E. Baudet, A. Kalendová, P. Benda and V. Nazabal, *Mater. Res. Bull.*, 2014, **51**, 176–179.
54 L. Ma, Y. Peng, Y. Pei, J. Zeng, H. Shen, J. Cao, Y. Qiao and Z. Wu, *Sci. Rep.*, 2019, **9**, 9503.
55 H. J. Stocker, *Appl. Phys. Lett.*, 1969, **15**, 55–57.
56 N. Yamada, E. Ohno, N. Akahira, K. i. Nishiuchi, K. i. Nagata and M. Takao, *Jpn. J. Appl. Phys.*, 1987, **26**, 61–66.
57 H. S. P. Wong, S. Raoux, S. Kim, J. Liang, J. P. Reifenberg, B. Rajendran, M. Asheghi and K. E. Goodson, *Proc. IEEE*, 2010, **98**, 2201–2227.
58 S. Raoux, W. Welnic and D. Ielmini, *Chem. Rev.*, 2010, **110**, 240–267.
59 T. Honma, Y. Benino, T. Fujiwara and T. Komatsu, *Appl. Phys. Lett.*, 2006, **88**, 231105.
60 T. Komatsu, R. Ihara, T. Honma, Y. Benino, R. Sato, H. G. Kim and T. Fujiwara, *J. Am. Ceram. Soc.*, 2007, **90**, 699–705.